

The Color of Water: Using Underwater Photography to Estimate Water Quality

John Breneman IV, Henryk Blasinski, Joyce Farrell

Department of Electrical Engineering, Stanford University, Stanford, CA, USA 94305

ABSTRACT

We describe a model for underwater illumination that is based on how light is absorbed and scattered by water, phytoplankton and other organic and inorganic matter in the water. To test the model, we built a color rig using a commercial point-and-shoot camera in an underwater housing and a calibrated color target. We used the measured spectral reflectance of the calibration color target and the measured spectral sensitivity of the camera to estimate the spectral power of the illuminant at the surface of the water. We then used this information, along with spectral basis functions describing light absorbance by water, phytoplankton, non-algal particles (NAP) and colored dissolved organic matter (CDOM), to estimate the spectral power of the illuminant and the amount of scattered light at each depth. Our results lead to insights about color correction, as well as the limitations of consumer digital cameras for monitoring water quality.

Keywords: Underwater color photography

1. INTRODUCTION

Those who venture below the surface of the ocean are privy to a magnificent seascape of colorful marine plants, coral, and fish. Unfortunately, to humans, whose eyes are adapted to viewing landscapes from above the water line, much of that color is lost. The sunlight that is filtered and scattered in the atmosphere [1] is further attenuated and scattered by water, phytoplankton and particulate matter [2]. This both changes the spectrum of the illumination underwater and reduces its intensity.

Despite these limitations, data obtained from underwater color photography can be an important indicator to an ecosystem's health. Living coral, for instance, absorb and reflect light differently than dead coral. The color of light at different depths might also be used as an indicator of mid-column phytoplankton activity. A quick internet search reveals thousands of underwater photographs that may contain clues regarding the status of the global underwater ecosystem.

Extracting this color information requires detailed models describing an illuminating light spectrum's evolution as it passes through seawater. The basic principles of the absorption of light in water are described by the Beer-Lambert law [2], but the specific absorption constants may vary by location and season. Furthermore, existing work measuring underwater illumination is either based on spectrophotometric measurements that ignore important scattering effects or depend entirely on simulation.

In this paper, we present a simple model for underwater illumination based on how light is absorbed and scattered by phytoplankton and other organic and inorganic matter in the water. To test the model, we built a color rig using a commercial point-and-shoot camera in an underwater housing and a calibrated color target. The rig was used to estimate the variation of illumination with depth near Stanford University's Hopkins Marine Station in Monterey CA.

2. UNDERWATER PHOGRAPHY SYSTEM MODEL

The system model for underwater photography describes the scene and its interaction with the camera. The scene itself is described by the complex interaction between light, media and objects. The spectral power of the light from the scene reaching the imaging sensor is determined not only by how light is reflected from the surfaces within a scene, but also by how light is absorbed and scattered by phytoplankton and other organic and inorganic matter in the water. To better analyze and process the camera image data, we wish to model the process by which an image is formed underwater.

2.1 Image Formation

The camera pixel values m_j of the j -th channel, typically $j \in (R, G, B)$, are classically predicted by a simple linear system with three elements: the spectral power distribution of the scene illumination, I_λ , the spectral reflectance of surfaces in a scene, r_λ and the spectral sensitivity of the imaging sensor, s_λ

$$m_j = g_j \Delta \sum_{\lambda=1}^N s_{j,\lambda} r_\lambda I_\lambda \quad (1)$$

The parameter g_j represents the scaling of the j -th channel. This scaling incorporates the overall effect of a number of parameters, including, but not limited to: ISO speed, aperture size and exposure duration. We further assume that the integration over continuous spectral power distributions is approximated with N discrete steps of width Δ .

Models used in imaging over long distances, for example in landscape photography, often incorporate additional terms that depend on the medium in which the light propagates, but are independent on the target surface reflectance [1]. Just as in landscape photography, an underwater image is primarily affected by two components [2]. The first one, called direct, is a result of the ambient illuminant interacting with the target and is identical to the classical linear model. The second term represents the scattering phenomena. Scatter is caused when light reflected from the colloidal particles suspended in water enters the camera directly, without interacting with the target

$$m_j = \underbrace{g_j \Delta \sum_{\lambda=1}^N s_{j,\lambda} r_\lambda I_{d,\lambda}}_{direct} + \underbrace{g_j \sum_{\lambda=1}^N s_{j,\lambda} I_{b,\lambda}}_{backscattered} \quad (2)$$

Note that $I_{d,\lambda}$ and $I_{b,\lambda}$ represent the different direct and backscattered light intensities, respectively.

2.2 Attenuation

Attenuation or absorption refers to the decay of light intensity as it passes through water. In underwater photography this process is responsible for reducing the amount of light that reaches some depth. Both water molecules and the particles dissolved in the water absorb light energy, a process described by the Beer-Lambert Law [2]

$$I_{d,\lambda} = I_{0,\lambda} e^{-\alpha_{\lambda} d} \quad (3)$$

where I_0 denotes the initial light intensity, I_d is the intensity of light that has traveled along a path of length d through a medium characterized by a non-negative absorption coefficient α . The subscript λ indicates spectral variability of the particular parameter. Since the absorption coefficient is wavelength dependent, the light traveling through a medium will not only be attenuated, but the shape of its spectral power distribution will also be altered. Subjectively, this change is perceived as a change of the illumination color. The exact nature of the spectral shape will depend on the cumulative effect of absorption coefficients at different depths.

2.3 Absorption coefficient

The value of the absorption coefficient is strongly dependent on the chemical composition of the medium. In the case of sea water, the four major contributors are: phytoplankton, α_ϕ , non-algal particles (NAP), α_{NAP} , colored dissolved organic matter (CDOM), α_{CDOM} and pure sea water, α_w [3].

$$\alpha_\lambda = \alpha_{\phi,\lambda} + \alpha_{NAP,\lambda} + \alpha_{CDOM,\lambda} + \alpha_{w,\lambda} \quad (4)$$

The values for all of the absorption coefficients except water exhibit some variation, depending primarily on the concentrations of the particle type but also on other physical parameters such as particle size, shape and in the case of phytoplankton, chlorophyll concentration. To maintain a relatively simple model, some assumptions regarding the coefficients are required.

The greatest variation in absorption coefficient is reported for phytoplankton. Even though the absorption curves for different types of phytoplankton exhibit some variation [4], they share certain similarities, for example peaks at about 450 and 675 nm. For our purposes, a general phytoplankton absorption curve was derived by averaging data from [4] where six different phytoplankton species absorption spectra were measured. Analogous analysis can be performed for the NAP and CDOM components. In fact, many studies model these components as decaying exponentials with different

rates of decay [5]. For the purposes of this model, data were averaged from [5] to form general bases for both CDOM and NAP. The measurements of the spectral absorption coefficient of pure seawater are very similar and our own measurements are consistent with what has already been published in the literature [6] [7]. The final absorption curves used for this analysis are shown in Figure 1 below, normalized for unit area

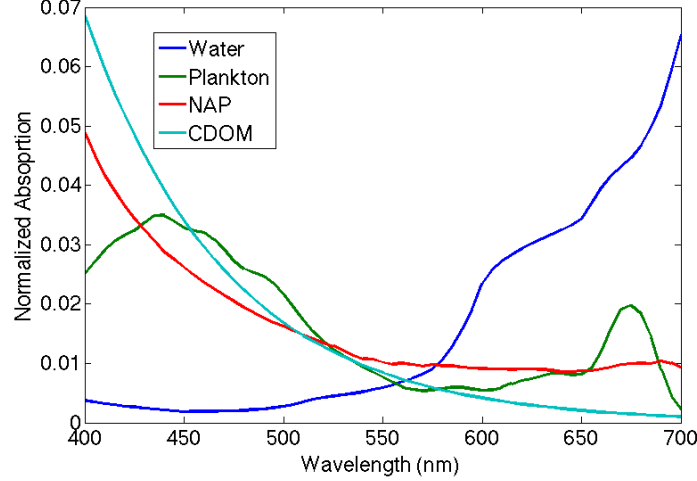


Figure 1. Normalized absorption basis functions.

The relative magnitudes of the absorption coefficients are determined by particulate concentrations. Defining concentration weights $c_{z,p}$ at the p -th depth D_p where $z \in \{\Phi, NAP, CDOM\}$, letting B_z refer to the normalized absorption curves, and dropping the implicit dependence on λ we have:

$$\alpha_p = B_\Phi c_{\Phi,p} + B_{NAP} c_{NAP,p} + B_{CDOM} c_{CDOM,p} + \alpha_w \quad (5)$$

To simplify the notation let us define $B = [B_\Phi \ B_{NAP} \ B_{CDOM}]$ and $c_p = [c_{\Phi,p} \ c_{NAP,p} \ c_{CDOM,p}]^T$. The absorption coefficient then becomes

$$\alpha_p = B c_p + \alpha_w \quad (6)$$

2.4 Backscatter

Backscatter refers to the light that enters a camera system directly, without interacting with any of the surfaces of the objects or calibration targets in an underwater scene. This light either originates in front of the camera's lens or is refracted into the lens by dissolved or suspended particulate matter in seawater. Its effects are independent of scene composition. In underwater photography, the backscatter effect is responsible for a green or blue "curtain" superimposed on images.

2.5 Simplified Model

The full image formation model, which includes both direct and backscattered terms, is complex and contains a large number of unknown parameters. Certain simplifying assumptions must be made. First, because the back-scattered component is independent of the calibration target, it can be represented in the model by $s_{j,\lambda} I_{b,\lambda}$. We represent backscattered term when summed over wavelengths as the constant $o_{j,p}$. Second, since the calibration target is close to the camera relative to the depth at which the image is taken, the attenuation of light is due primarily to the water column between the target and the imager. Incorporating these assumptions into the original image formation model, we now express the value acquired by the j -th camera channel at depth D_p as

$$m_j(D_p) = g_j \Delta \sum_{\lambda=1}^N s_{j,\lambda} r_\lambda I_{0,\lambda} e^{-D_p \alpha_\lambda} + o_{j,p} \quad (7)$$

The simplified model assumes surface illuminant propagation through an absorptive medium. Although the phytoplankton concentration across depth may not be constant [8], the model uses the average absorption coefficient for a layer of total thickness D_p .

3. MODEL PARAMETER ESTIMATION

The surface illuminant I_0 and underwater parameters, c_p and $o_{j,p}$, are estimated independently. First I_0 is estimated using an image of a target with known surface reflectances captured above the water's surface. The estimate of I_0 is then used in the simplified image formation model to estimate the absorption and scattering coefficients, c_j and $o_{j,p}$, at a given depth via iterative Taylor series expansion.

3.1 Surface Illuminant

Natural illuminants are smoothly varying functions of wavelength and therefore can be compactly represented with a small number of basis functions. For example, the spectral power in natural daylight illumination can be described by a weighted combination of only three spectral basis functions [9, 10]. The image formation model at the surface therefore becomes

$$m_j = g_j \Delta \sum_{\lambda=1}^N s_{j,\lambda} r_\lambda B_D \gamma$$

$$I_0 = B_D \gamma$$
(8)

where B_D is a matrix of daylight basis functions and γ is the unknown weight vector. If k different reflectance targets are observed with a j channel camera registering values $m_{j,k}$, then the parameters γ can be found by solving a linear equation

$$\underset{\gamma}{\text{minimize}} \sum_{j,k} \left| m_{j,k} - g_j \Delta \sum_{\lambda=1}^N s_{j,\lambda} r_{k,\lambda} B_D \gamma \right|^z$$
(9)

If $z = 2$ then Equation 9 above becomes a least-squares problem and a closed form solution exists. Alternatively other values of z can be selected to reduce the influence of outliers and additional constraints, such as smoothness, can be introduced to further constrain the solution. In these cases iterative algorithms will be required.

3.2 Absorption and Scatter

When the surface illuminant I_0 is known, the simplified image formation model equation becomes convex in parameters $o_{j,p}$ and c_p . Furthermore, the function is monotonically decreasing in $\alpha_{p,\lambda}$ which in turn are linear functions of c_p . For these reasons, at fixed values D_p the norm

$$\left| m_j - g_j \Delta \sum_{\lambda=1}^N s_{j,\lambda} r_\lambda I_{0,\lambda} e^{-\alpha_{p,\lambda} D_p} + o_{j,p} \right| \quad \alpha_{p,\lambda} = (B c_p + \alpha_w)_\lambda$$
(10)

is a quasi-convex function with a global minimum attained at c_p^* and $o_{j,p}^*$.

We estimate the scatter and absorption model parameters independently at each depth. Starting at the first depth measurement, $p = 1$, the optimal parameter set is found by iteratively solving a model linearized around the estimate at iteration (t) of the parameter $c_p^{(t)}$ using Taylor series expansion. The result from the previous iteration is used as the center point for the Taylor Series expansion in the next iteration and the process is run until convergence. The algorithm may be summarized as follows:

- Select a starting point $c_p^{(0)} = \mathbf{1}$, $p = 1$.
- Iteratively solve the linearized optimization problem over $c_p^{(t+1)}$ and $o_{j,p}$ until convergence

$$\begin{aligned}
c_p^{(t+1)} &= \operatorname{argmin} \sum_{j,k} |m_{j,k} - F_{j,k}(c_p^{(t)}) - \nabla F_{j,k}(c_p^{(t)})(c_p^{(t+1)} - c_p^{(t)}) - o_{j,p}| \\
\text{subject to} \quad B_\Phi c_{\Phi,p}^{(t+1)} &\geq 0 \quad B_{NAP} c_{NAP,p}^{(t+1)} \geq 0 \quad B_{CDOM} c_{CDOM,p}^{(t+1)} \geq 0
\end{aligned} \tag{11}$$

where

$$F_{j,k}(c_p^{(t)}) = g_j \Delta_\lambda \sum_{\lambda=1}^N s_{j,\lambda} r_{k,\lambda} I_{0,\lambda} e^{-\left(B c_p^{(t)} + \alpha_w\right)_\lambda (D_p)} \tag{12}$$

$$\nabla F_{j,k}(c_p^{(t)}) = g_j \Delta_\lambda \sum_{\lambda=1}^N s_{j,\lambda} r_{k,\lambda} I_{0,\lambda} B_\lambda e^{-\left(B c_p^{(t)} + \alpha_w\right)_\lambda (D_p)} \tag{13}$$

- Repeat the second step until all P depth levels have been analyzed.

Note that $m_{j,k}$ represent the measured sensor values of the k -th target in the j -th channel at the p -th depth level. The subscript p is ignored for convenience. The inequality constraint introduced in the optimization problem follows from the non-negativity of the absorption coefficient values.

The convergence of this algorithm is guaranteed by the properties of convex functions. To confirm this, a numerical stability was empirically verified using data simulated according to this model and solving for the unknown parameters. Estimation error levels were comparable to the numerical precision.

4. DATA COLLECTION

To test our model for underwater illumination we constructed a color rig using a commercial point-and-shoot camera, a Canon SX260HS, in an underwater housing and an XRITE color target. The XRITE color target was chosen primarily because it is widely used and easily obtainable. Although the XRITE color patches themselves are not linearly independent in the spectral space, they easily cover the spectral extent of the camera's color filter sensitivities and provide a sufficient basis for estimating the relative weights of the four absorption basis functions. The color target was enclosed within a polycarbonate case to protect against the harsh underwater environment.

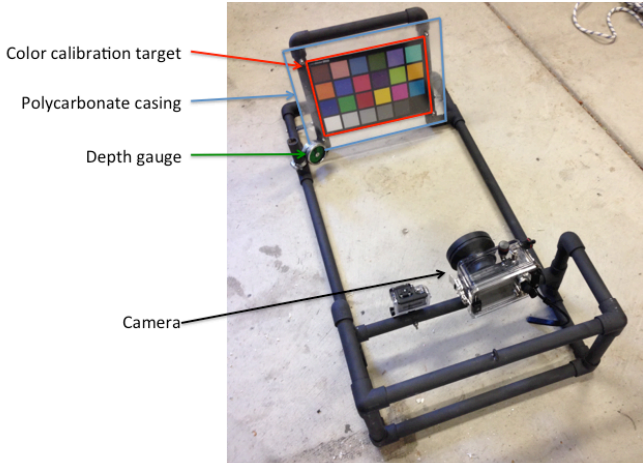


Figure 2. Underwater rig for color photography. The color calibration target was an XRITE ColorChecker (formerly known as the Macbeth ColorChecker). The calibration target was enclosed in a waterproof polycarbonate casing. A depth gauge was visible in all camera images in order to record the depth at which each image was captured. The rig was designed to minimize specular highlights and shadows.

4.1 Camera

An alternative firmware for the camera, CHDK[11] was loaded to allow access to the raw image sensor data and to program the camera to take a series of photos at a predefined interval. The camera was configured to operate in aperture-priority mode while the exposure duration and ISO-sensitivity were selected automatically using the camera's light meter.

4.2 Spectral Sensitivity

To measure the spectral response of the SX260HS, the camera was exposed to a series of narrowband lights created by a Newport Oriel Cornerstone 130 monochromator. The spectral radiance of each of the narrowband lights was measured by a Photo Research PR-650 colorimeter and entered into an $N \times M$ matrix (L), where N is the number of wavelength samples and M is the number of spectral lights. The camera RGB images for each of the narrowband lights were normalized for differences in exposure duration and gain. The corrected RGB values for each of the M lights forms a $3 \times M$ matrix (C). We estimated the channel spectral sensitivity by using a robust method to solve for S in the linear equation: $C = S'L$.

4.3 Color Target Reflectivities

The color patch reflectance values for the XRITE color checker are well known but the target is enclosed in polycarbonate on the underwater color rig. To verify the polycarbonate has a negligible effect, the reflectance values were re-measured using the PR-650 colorimeter and a calibration light box. The reflectance values measured match those published in other works, with a slight notch around 675nm, indicating only slight effects due to the polycarbonate.

4.4 Underwater Data

Several generations of the color rig were tested on dives near Stanford's Hopkins Marine Station in Monterey Bay, CA. Fifteen of the dives were conducted using the final index-compensated underwater color rig. Two of the dives were selected for analysis: a dive under typically murky underwater conditions and a dive under extraordinarily clear underwater conditions. Each dive produces a set of RGB sensor values observed by the camera for each of the 24 color patches along with a depth measurement. The sensor values were adjusted for the exposure and camera ISO sensitivity values and converted into normalized RGB values that were linear with intensity.

5. RESULTS

All the algorithms were implemented in MATLAB using the CVX convex optimization toolbox [12]. In order to decrease the sensitivity to outliers, l_1 norms were used as penalties. Iterative algorithms had an upper limit of 100 iterations imposed, however in all cases the convergence was achieved well ahead of this limit.

5.1 Surface Illuminant

Three daylight basis functions were used in the surface illuminant computations (see Equation 8). Figure 3 shows the normalized spectral power distributions of the illuminant computed for the murky and clear water dives. Their shapes are similar to the CIE standard daylight illuminant D65.

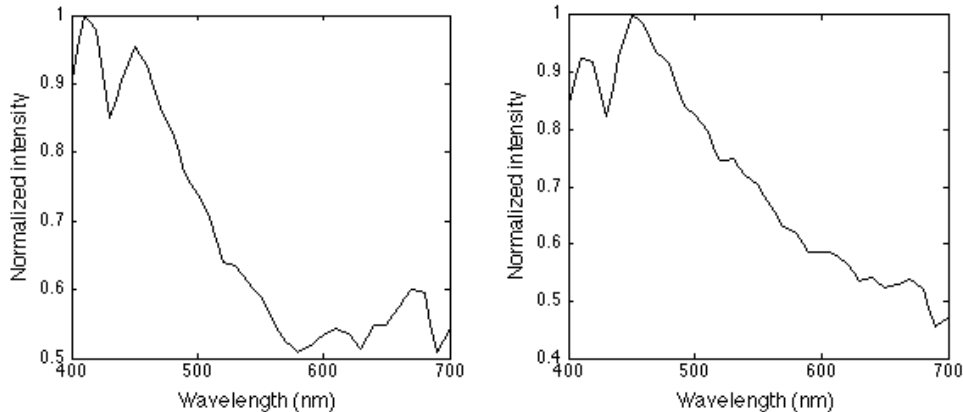


Figure 3. I_0 estimates for the murky dive (left) and clear dive (right)

5.2 Absorption and Scatter

The estimates of I_0 were used in the simplified image formation model to estimate the values of the absorption coefficients and scatter offset constants for the murky and clear water dives. The contributions $W_z(D_p)$ at each depth were averaged over all the wavebands according to:

$$W_z(D_p) = \frac{\sum_{\lambda=1}^N \alpha_{z,\lambda,p}}{\sum_{\lambda=1}^N \alpha_{\lambda,p}} \quad (14)$$

Several trends are apparent in the absorption coefficients fit by the model. First, there is a dramatic difference in the relative role of water in the overall absorption coefficient. In the murky water dive less than 5% of the overall attenuation of light is attributed to water. In the clear water dive, light attenuation was primarily due to water at all depths except those greater than 18m. The increase in the clear dive CDOM contributions at depths greater than 18m suggests the rig entered a layer of increased particulate concentration. Such layers are common on calm days in Monterey due to the establishment of an oceanic temperature inversion layer [13].

Second, there is a high variation in NAP and CDOM absorption estimates in the model while phytoplankton is attributed with very little of the absorption coefficient. It is unlikely, however, that the phytoplankton absorption coefficient would be largely nonexistent on a typical dive in murky water. More likely, the estimates of NAP and CDOM included contributions by the absorption of phytoplankton. This is because the camera has very little sensitivity at the short and longer wavelength regions (see Figure 1). Consequently, the camera cannot discriminate between spectral absorption of phytoplankton and NAP and CDOM in the short wavelengths and the absorption of phytoplankton and water at the longer wavelengths. In the future, we plan to use simulations to determine whether it is possible to detect the amount of phytoplankton by removing the camera IR filter.

The model estimates for scatter offsets quantify the salient effect that scatter has on underwater color photography. Since the sensor values were converted into normalized values that were linear with intensity the estimates of scatter offset are also in units that are linear with intensity. The effect of scattered light on the camera can be estimated by dividing the scatter offset by the camera values for any color patch (also converted to units of intensity). This analysis reveals that light scatter has a significant effect on the camera images of all color patches at all depths. For example, in the case of the murky water dive, light scatter accounts for 15% of the intensity of the white patch (with a neutral density of 9.5) and 43% of the intensity of a gray patch (with a neutral density of 5) at a depth of 15 meters. For the clear water dive, light scatter accounts for 16% of the intensity of the white patch and 58% of the intensity of the same gray patch at the same depth (15 meters).

5.3 Model accuracy

The mean relative prediction error between the model and acquired values can be computed at specific depth p by

$$\text{error}(D_p) = \frac{1}{N} \sum_{j,k} \frac{|m_{j,k,p} - \hat{m}_{j,k,p}|}{m_{j,k,p}} \quad (15)$$

where $\hat{m}_{j,k,p}$ is the value returned by the model evaluated at the optimal absorption and scattering parameters parameters c_p^* and $o_{j,p}^*$ at depth p . In most cases, the prediction error averages 20%. Although this is a relatively high error, it is comparable to errors computed while calibrating the camera under extremely low light conditions.

Visually, the results produced by the model are also comparable to the empirical data we collected with the underwater color photography rig. Figures 4 and 5 present side by side comparisons of the Macbeth color checker patches acquired during the experiment, and generated from the model with optimally selected absorption and scatter parameters. Note that only one sample per patch was analyzed and the patch area has been enlarged for visual convenience. The two images are taken from the two data sets, and they were acquired at two different depths. The figures illustrate that the model is able to capture the characteristic greenish tint of the murky water (Figure 4) and the bluish tint of the clear water (Figure 5).

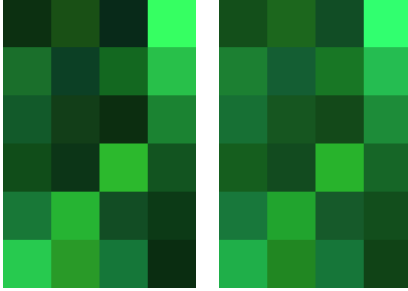


Figure 4. Measured (left) and predicted (right) camera RGB values for murky water at 21 meters.

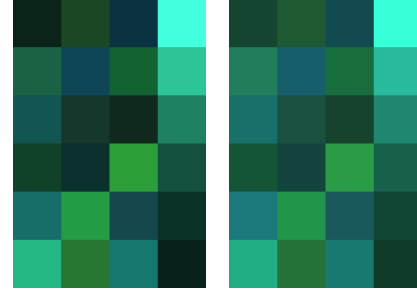


Figure 5. Measured (left) and predicted (right) camera RGB values for clear water at 9 meters.

5.4 Impact On Color Photography

Digital cameras typically perform an initial color balancing operation to map the camera's linear RGB sensor values into the linear display RGB values (sRGB) that would be generated if the calibration target were illuminated with D65 daylight. Conventionally, this color balancing is implemented as a 3x3 linear transform, as shown below in matrix tableau below, with values c chosen to transform camera sensor values $[R_c \ G_c \ B_c]$ from a scene into known linear sRGB display values $[R_d \ G_d \ B_d]$.

$$\begin{bmatrix} R_d \\ G_d \\ B_d \end{bmatrix} = \begin{bmatrix} c_{11} & c_{12} & c_{13} \\ c_{21} & c_{22} & c_{23} \\ c_{31} & c_{32} & c_{33} \end{bmatrix} \begin{bmatrix} R_c \\ G_c \\ B_c \end{bmatrix} \quad (16)$$

The XRITE color target used in the underwater rig has well known linear sRGB patch values under the D65 illuminant. Comparing the RGB sensor values received by the camera to the ideal XRITE sRGB values, we can compute the weights c that produce linear sRGB values as close as possible, by L_1 norm, to the ideal values. The results of performing a 3x3 color transform containing such weights c on two images from the murky dive are rendered below in Figure 6.

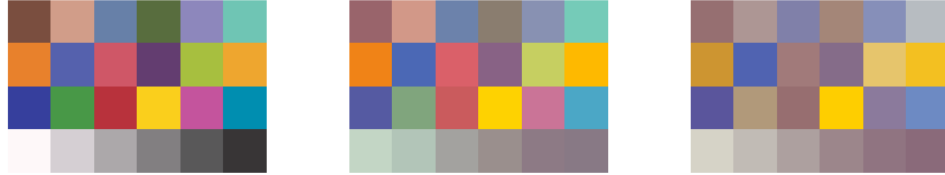


Figure 6 - Reference colors (left) and optimal 3x3 color balancing applied at 5 meters (middle) and 20 meters (right)

Figure 6 illustrates the finding that the optimal 3x3 color balancing transform for the murky dive data taken at 5 meters performs better than the optimal 3x3 color balancing transform for the murky dive data obtained at 20 meters. In general, the 3x3 color balancing transforms worked better for murky water images taken at depths shallower than 5-10 meters but failed at greater depths. A significant factor contributing to this failure is the percentage of scattered light that enters the camera. This additional light source is not modeled well by a 3x3 color balancing transform. However, because light scatter creates a global, scene independent offset in color values, we can define a new 3x4 affine color balancing transform to include an offset term for each color channel as shown below:

$$\begin{bmatrix} R_d \\ G_d \\ B_d \end{bmatrix} = \begin{bmatrix} c_{11} & c_{12} & c_{13} & c_{14} \\ c_{21} & c_{22} & c_{23} & c_{24} \\ c_{31} & c_{32} & c_{33} & c_{34} \end{bmatrix} \begin{bmatrix} R_c \\ G_c \\ B_c \\ 1 \end{bmatrix} \quad (17)$$

Again, using the known linear sRGB color patch values of the XRITE color checker, we compute an optimal 3x4 color transform as measured by L_1 norm for the same images. The results are rendered in Figure 7 below. The 3x4 transform performs better for both the 5-meter and 20-meter images, indicating that color balancing transforms intended for underwater use must account for significant backscatter contributions. The 3x4 transform does not perform well at all

depths, notably along the third row of the 20-meter image, but it represents a significant improvement in the images collected in murky water.

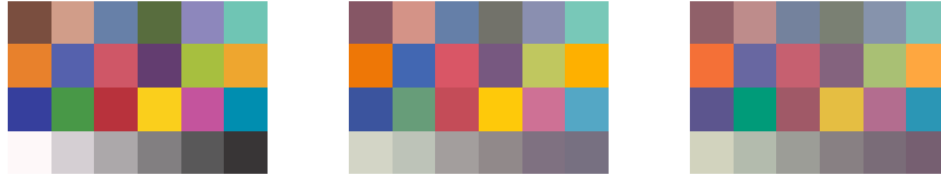


Figure 7. Reference colors (left) and optimal 3x4 color balancing applied at 5m (middle) and 20m (right)

The image formation model predicts that both 3x3 and 3x4 linear color transforms will fail under clear water conditions. Despite the significantly smaller attenuation coefficient of clear water, the underwater illumination in clear water suffers from color filter limitations in the camera. Figure 8 shows the illuminant in murky water predicted by the estimated attenuation coefficients α_z at a depth of 15 meters. The illuminant and camera spectral sensitivities have been normalized to unit magnitude.

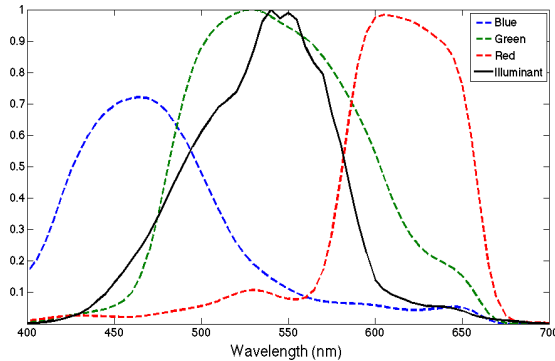


Figure 8. Camera sensitivity and murky water illuminant at 15 meters

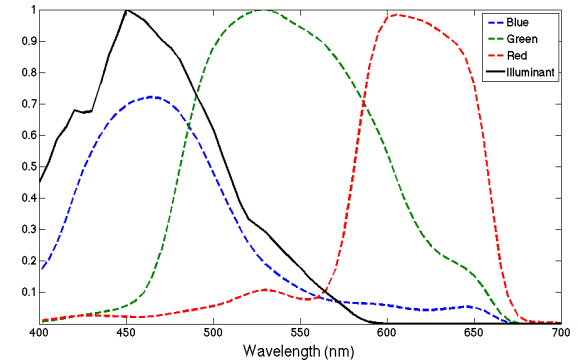


Figure 9. Camera sensitivity and clear water illuminant at 15 meters

The murky water illuminant has a strong peak at 550nm but still has observable energy in the range of the camera's red channel. Compare this with the clear water illuminant predicted by the estimated attenuation coefficients α_z at a depth of 15 meters, shown in Figure 9 above. The clear water illuminant exhibits a strong peak at 450nm and drops to near zero around 600nm. Very little of the red channel's response is due to wavelengths above 600nm. Since the distinction between many of the color patches in the color target lie above 600 nm, it is no longer possible to re-create this information. Indeed, an optimal 3x4 color transform applied to the 15-meter clear water image fails to accurately reproduce the color target, as shown in Figure 10 below.

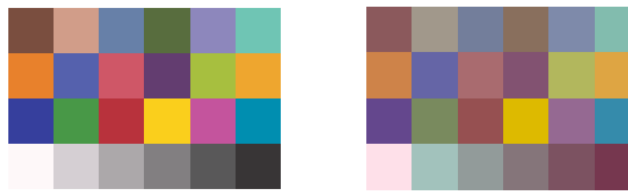


Figure 10. Reference colors (left) and optimal 3x4 color balancing applied to image data captured at 15 meters during the clear water dive

Currently, the solution used by underwater photographers is to introduce an external filter that reduces the amount of blue and green wavelengths entering a camera, bringing them closer to the range of ambient red wavelengths. This scheme works well at certain depths, but the filters are not able compensate for changes in depth and must be changed whenever the camera's depth changes.

6. DISCUSSION AND SUMMARY

The color of water is determined by how light is absorbed and scattered by the substances in water. To understand this process, we developed a model for underwater illumination that uses spectral functions describing the absorbance of light by water, phytoplankton and other organic and inorganic matter in the water. To test the model, we built a color rig using a commercial point-and-shoot camera in an underwater housing and a calibrated color target. We used the measured spectral reflectance of the calibration color target and the measured spectral sensitivity of the camera to estimate the spectral power of the illuminant at the surface of the water. We then used this information, along with spectral basis functions describing light absorbance by water, phytoplankton, non-algal particles (NAP) and colored dissolved organic matter (CDOM), to estimate the spectral power of the illuminant and the amount of scattered light at different depths in water.

The model estimates for scatter in underwater photography suggest that light scatter contributes at least 15% of the color signal reaching the camera and, in some cases, can contribute as much as 50% of the color signal. Traditional 3x3 color transforms will not work well in the presence of scatter. We can, however, define a new 3x4 affine color balancing transform to include an offset term for each color channel and do a much better job at color correction.

The model estimates for the spectral power of the underwater illuminants reveal additional insights about color correction for underwater photography. The presence of particulates in murky water acts as a filter reducing the gain on the blue and green color channels. Ironically, this has a beneficial result because it enables the camera to capture a higher SNR signal in the red color channel. When these particulates are not present in the water, as in the case of the clear water dive, the red channel's signal is dominated by the signal in the shorter blue and green wavelengths. This results in a poor or no "real" 600nm signal in the red color channel. Under these circumstances, the RGB camera acts as a GB camera and neither a 3x3 or a 3x4 transform can correct the images.

A conventional way to handle the imbalance of signals in the red, green and blue channels is to place a color filter in front of the camera that transmits light well in the longer wavelengths and reduces the light in the shorter wavelengths. The problem with this solution is that a filter may work well for one condition (clear water) but not in other conditions. Moreover, the filter reduces signal in a situation where there is already very little light available. Ideally, one would like to be able to dynamically modulate the red, green and blue color channels. This is, of course, difficult if not impossible to do with consumer digital cameras. Another approach might use a nonlinear color transform to infer the missing spectral content.

Our analysis of images captured with our underwater color photography rig also gave us insights into the challenges in monitoring the quality of water using consumer digital cameras that have an IR filter. The spectral sensitivity of these cameras makes it impossible to discriminate between light attenuation due to phytoplankton and any of the other components. The cameras have no sensitivity in the short wavelength region where the light absorbance by phytoplankton is different from the light absorbance by NAP and CDOM. They are also blind in the longer wavelengths where the light absorbance by phytoplankton differs from the light absorbance by water. Perhaps by removing the IR filter, it will be possible to distinguish between attenuation due to water and attenuation due to phytoplankton.

Finally, the combination of our modeling and empirical data collection lead us to the conclusion that much can be gained by computer simulations of the complete imaging pipeline for underwater photography. The predictions of our model for underwater illumination are qualitatively consistent with what we observe in the empirical data. This makes us more confident that this model, in combination with software for simulating digital cameras [14] [15], will enable us to prototype changes in camera design and image processing methods in order to improve the quality of the images and the data we capture underwater.

7. ACKNOWLEDGMENTS

The authors wish to thank Charles VanGorkum Jr. for assistance in the design and assembly of the underwater color rig and John W. Breneman III for assistance collecting underwater dive data. We also thank Colin Roesler, Annick Bricaud and Tetsuichi Fujiki for providing the numerical data used in their respective papers, and Sumit Chawla for his advice and encouragement.

8. REFERENCES

- [1] Narashimhan, S.G. and S.K. Nayar, *Vision and the Atmosphere*. International Journal of Computer Vision, 2002. **48**(3): p. 233 – 254.
- [2] Bofferty, M., F. Galland, and A. Allais, *Color image simulation for underwater optics*. Applied Optics 2012. **51**(23): p. 5633 – 5642.
- [3] Babin, M., et al., *Variations in the light absorption coefficients of phytoplankton, nonalgal particles, and colored dissolved organic matter in costal waters around Europe*. Journal of Geophysical Research, 2003. **108**(C7).
- [4] Fujiki, T. and S. Takaguchi, *Variability in chlorophyll a specific absorption coefficient in marine phytoplankton as a function of cell size and irradiance*. Journal of Plankton Research, 2002. **24**(9): p. 859-874.
- [5] Bricaud, A., et al., *Variations of light absorption by suspended particles with the chlorophyll a concentration in oceanic (Case 1) waters: analysis and implications for biological models*. Journal of Geophysical Research, 1998. **103**(C13): p. 31033 – 31044.
- [6] Hale, G.M. and M.R. Querry, *Optical constants of water in the 200-nm to 200-um wavelength region*. Applied Optics, 1973. **12**(3): p. 555 – 563.
- [7] Smith, R.C. and K.S. Baker, *Optical properties of the clearest natural waters (200 – 800 nm)*. Applied Optics, 1981. **20**(2): p. 177-184.
- [8] Ballesteros, D., *Remote sensing of vertically structured phytoplankton pigments*. Topicos Meteorologicos y Oceanograficos, 1999. **6**(1): p. 14 – 23.
- [9] D. B. Judd, D.L. MacAdam, and G. Wyszeski, *Spectral distribution of typical daylight as a function of correlated color temperature*. Journal of the Optical Society of America, 1964. **54**: p. 1031-1040.
- [10] DiCarlo, J.M. and B.A. Wandell, *Spectral estimating theory: beyond linear but before Bayesian*. J. Opt. Soc. Am A, 2003. **20**(7): p. 1261-1270.
- [11] Canon Hack Development Kit. December 2012]; Available from: <http://chdk.wikia.com/wiki/CHDK>.
- [12] CVX Research, I. *CVX: Matlab software for disciplined convex programming, version 2.0*. April 2011; Available from: <http://cvxr.com/cvx>.
- [13] Krauss, J.A., *Introduction to Physical Oceanography*2005: Waveland Press, Inc. . 309.
- [14] Farrell, J., et al., *A simulation tool for evaluating digital camera image quality*. Proceedings of the SPIE, 2004. **5294**: p. 124-131.
- [15] Farrell, J.E., P.B. Catrysse, and B.A. Wandell, *Digital camera simulation*. APPLIED OPTICS, 2012. **51**(4).